Three-dimensional microstructure-explicit and void-explicit mesoscale simulations of detonation of HMX at millimeter sample size scale

Christopher Miller, Daniel Olsen, Yaochi Wei, et al.

View Online   Export Citation   CrossMark

ARTICLES YOU MAY BE INTERESTED IN

Understanding the shock and detonation response of high explosives at the continuum and meso scales
Applied Physics Reviews **5**, 011303 (2018); https://doi.org/10.1063/1.5005997

Direct numerical simulation of shear localization and decomposition reactions in shock-loaded HMX crystal
Journal of Applied Physics **117**, 185902 (2015); https://doi.org/10.1063/1.4918538

Quantification of probabilistic ignition thresholds of polymer-bonded explosives with microstructure defects
Journal of Applied Physics **124**, 165110 (2018); https://doi.org/10.1063/1.5031845

Three-dimensional microstructure-explicit and void-explicit mesoscale simulations of detonation of HMX at millimeter sample size scale

View Online   Export Citation   CrossMark

Christopher Miller,   (iD)   Daniel Olsen, Yaochi Wei, and Min Zhou[a]   (iD)

AFFILIATIONS

The George W. Woodruff School of Mechanical Engineering and The School of Materials Science and Engineering,
Georgia Institute of Technology, Atlanta, Georgia 30332-0405, USA

[a]**Author to whom correspondence should be addressed:** min.zhou@gatech.edu

ABSTRACT

Fully three-dimensional (3D) microstructure-explicit and void-explicit mesoscale simulations of the shock-to-detonation (SDT) process of pressed granular HMX (octahydro-1,3,5,7-tetranitro-1,3,5,7-tetrazocine) are performed. The overall size scale of the models is up to $3 \times 3 \times 15 \ mm^3$, with ~30 000 grains and 206 265 voids. The models account for the heterogeneous material microstructure, constituent distribution, constituent morphology, and voids. Loading conditions considered involve piston velocities in the range of 600–1200 m/s or pressures in the range of 4–8 GPa. The focus is on analyzing the SDT process and the effects of microstructure and voids on the run-to-detonation distance (RDD). Companion two-dimensional (2D) simulations are also carried out to assess the differences between 2D and 3D. Statistically equivalent microstructure sample sets (SEMSSs) are generated and used for both 2D and 3D, allowing the prediction of the statistical and probabilistic Pop plots (PPs). The predictions are in general agreement with trends in available experimental data in the literature. It is found that both the microstructure (heterogeneous grain size, morphology, and size distribution) and voids significantly affect the RDD and the PPs. These effects are systematically delineated and quantified via the use of SEMSSs with different combinations of attributes. A recently developed probabilistic formulation for the PPs is used to characterize the results, allowing uncertainties in the relations between the shock pressure and RDD arising from material heterogeneities to be quantified. The probabilistic formulation is further used to quantify the confidence levels in the ranked order of influences of different combinations of microstructure and voids on the PPs.

Published under license by AIP Publishing. https://doi.org/10.1063/1.5136234

I. INTRODUCTION

Understanding the effects of microstructure heterogeneities on the shock-to-detonation transition (SDT) behavior of high explosives (HEs) has remained a long-standing challenge to the energetic community at large. With the ever increasing prominence of high performance computing (HPC) and the development of material models, increasingly sophisticated simulations are able to capture local material behavior that remains difficult to study experimentally. An accurate understanding of the evolution of temperature and pressure fields accounting for underlying mechanical, thermal, and chemical processes in a material subject to shock loading is critical to the prediction of the behavior of HEs. As such, there have been extensive simulations on local mesoscale behavior.[1–6]

The most commonly accepted ignition theory involves recognizing the development of hotspots or localized areas of high temperatures. These hotspots lead to the onset of chemistry[4,7–9] and are often the result of localized mechanical energy dissipation, usually due to the presence of material defects or microstructure heterogeneities. Once ignition occurs, chemistry leads to thermal runaway, resulting in melting and transformation to gas phases. This chemical process is accompanied by intense and rapid pressure increases, which cause shockwaves to radiate from the hotspot ignition sites, leading to criticality at other sites. This avalanche event ultimately results in the formation of a detonation wave and the SDT when the detonation front catches up with the shock front. The distance the shock wave front travels before being overtaken by the detonation wave front is known as the run distance to detonation or run-to-detonation distance (RDD) and is a common metric used in the form of a Pop plot (PP)[10] to gauge the detonation sensitivity of an HE.

The effects of chemical reactions are often represented by Arrhenius-type kinetics models,[11] which are calibrated using experimental data,[12,13] density functional theory (DFT)/chemical kinetics calculations,[14,15] and results of molecular dynamics simulations.[16] For example, Mader[17] modeled detonation initiation and propagation of homogeneous HEs along surfaces. Since the time rates of changes of physical quantities in a detonation are extremely high and the RDDs for different materials are on the order of millimeters, very short time steps and large sample sizes are required to capture the full shock loading, development of hotspots, hotspot ignition, formation of detonation, and the ultimate SDT, making simulations very computationally expensive. For heterogeneous materials, the challenge is even more formidable because very fine meshes are required to resolve material microstructure and defects such as voids. For these reasons, fully resolved mesoscale simulations of SDT at overall sample sizes on the order millimeters have been rare. To partly circumvent this computational issue, phenomenological models have been used. One such model is the ignition and growth model of Lee and Tarver.[18,19] This approach relates the chemical reaction rate to the local pressure and reaction progress variables. Other common models include the Forest Fire[20,21] and JTF (Johnson-Tang-Forest)[22] models. These reactive burn models have become a common tool for simulating detonation at reasonable computational cost, as they do not account for microstructure morphology. The history variable reactive burn (HVRB) model expresses the chemical reaction rate as a function of a time integral of the local pressure in the material.[23,24] These models are just a few examples of the many ways[25–31] to account for the effects of chemical reactions, the formation of detonation waves, and the SDT. There is a common trade-off between accuracy and simulation time or simulation scale. Our focus here is not on the differences among different chemistry models, but rather the development of a 3D mesoscale approach that reaches the macroscale. Therefore, the model here can be regarded as one that bridges the mesoscale and the millimeter level macroscale.

Mesoscale models, to various degrees, resolve material heterogeneities, defects, and hotspot development under conditions of various mechanical, thermal, or electromagnetic excitations.[32–38] The energetic community has been developing new ways to characterize microstructure and microstructure effects on the ignition and detonation of HEs. A few are mentioned here as examples. Wei et al.[39] studied the effects of material defects in the forms of interfacial debonding and grain cracks using a cohesive finite-element based Lagrangian approach. Miller et al.[40] studied the effects of aluminum particles on the sensitivity of polymer-bonded explosives (PBXs). Rai et al.[41] analyzed the collapse of a void under shock loading using an Eulerian framework. Austin et al.[42,43] used an arbitrary Lagrangian-Eulerian approach (ALE3D) to study melt lines and shear banding following pore collapse. Yarrington et al.[44] studied the SDT in HNS (2,2′,4,4′,6,6′-hexanitrostilbene), accounting for a large population of randomly distributed nanopores whose statistical attributes track those of an experimentally scanned sample. The predicted threshold velocity required to cause detonation matches the experimental measurement. The success can be partly attributed to the resolution of the mesoscale void structure and the calibration of the chemistry model to MD data.[16] These models are generally 2D and at the overall sample scale of micrometers or tens of micrometers.

Baer et al.[45] were the first to carry out 3D simulations using CTH, the Sandia National Labs solid mechanics code. The analysis concerned the compaction of granular HMX in a cubic millimeter volume consisting of approximately 1900 grains under a loading piston speed of 1000 m/s. The local pressure-based HVRB model was used to simulate reaction. Due to computational cost, the calculations at lower load intensities could not be continued long enough to reach SDT. Reaugh[46] used ALE3D to analyze the response of a $300 \times 300 \times 300 \, \mu m^3$ block of PBX and found that a pressure-dependent deflagration chemistry model yielded better results than an Arrhenius-type hotspot growth model. Recently, Rai and Udaykumar[47] modeled the local effects of pore collapse in a homogeneous 3D HMX block $1.3 \times 4 \times 12 \, \mu m^3$ in size and found higher sensitivity in 3D than in 2D. Jackson et al.[48] used a phenomenological model with energy deposition representing the effect of voids to study the effects of shock pressure on ignition times in a PBX setting without explicitly resolving voids.

Due to computational cost, much of the work in the energetic community so far uses two-dimensional frameworks and involves various degrees of homogenization or phenomenological treatment. To more realistically capture the 3D nature of material microstructure and heterogeneous configurations, to resolve the length scale of physical events, such as the SDT of HE under shock loading, and to directly bridge the mesoscale and the macroscale, there is a strong need for fully 3D models that explicitly resolve mesoscale material structures (microstructures or material heterogeneities, voids) as well as relevant thermo-mechano-chemical processes. Ultimately, such 3D models can also shed light on if and how 2D and 3D models differ as well as possible inadequacies of 2D models.

In this paper, we present fully dimensional (3D) microstructure-explicit (ME) and void-explicit (VE) mesoscale models at the millimeter scale for pressed granular HEs under shock loading. Both material microstructures and voids are explicitly resolved. The overall size scale of the models is up to $3 \times 3 \times 15 \, mm^3$, large enough to resolve the full process from the onset of loading to eventual SDT with the detonation front propagating in the remaining un-shocked part of the material. At the largest size scale, the samples have ∼30 000 grains and 206 265 voids. The processes captured include thermal-mechanical response, the onset of chemical reaction, the formation of a detonation front, and the SDT. In the calculations carried out, the particular material of choice is HMX (octahydro-1,3,5,7-tetranitro-1,3,5,7-tetrazocine). Four model cases are considered: homogenous material with no microstructure or voids, material with a granular microstructure but no voids, material with voids but no microstructure, and material with both voids and granular microstructure. Shock loading is generated by an aluminum flyer thick enough to maintain continuous loading on the HMX sample without unloading. The focus of the analyses is on the SDT process and the RDD, rather than the details of local fields in the material. Statistically equivalent microstructure sample sets (SEMSSs) for the heterogeneous cases are used, allowing probabilistic quantification of the PPs and statistically significant assessment of the rank order of the influences of different material factors (microstructure, voids, and combinations thereof). The results from 2D and fully 3D simulations are compared to outline their potential differences and highlight factors that should be addressed in

the future for more systematic comparisons and assessment of the multi-dimensional models.

The quantification of the probabilistic nature or uncertainties uses the statistical approach first proposed by Wei et al.[49] for detonation thresholds and later expanded by Miller et al.[50] This analysis results in the generation of probabilistic Pop plots along with analytical relations. These relations can also be used to determine the necessary shock pressure, run distance, or SDT probability given any two of the three quantities. The relations also allow pressure-dependent confidence levels to be established in the comparisons of the Pop plots for different materials. Although the material of focus is HMX, the models, the approach, and the analytical relations developed are applicable to PBXs and other energetic materials.

II. Framework of analysis

The 3D simulations are carried out using CTH, the Sandia National Labs solid mechanics code. Sustained loading is effected on the sample via the use of a thick aluminum flyer with velocities varying from 600 m/s to 1200 m/s, resulting in shock pressures between 4 and 8 GPa. In Sec. II A, the method for generating 3D SEMSSs is discussed. An outline of the constitutive models used is given in Sec. II B. The results of mesh convergence and sample size effects are discussed in Sec. II C.

A. Material, model, and microstructure

In order to accurately quantify the effects of microstructure heterogeneities on the detonation behavior, we consider four types of samples: homogenous (H), microstructured without voids (M), homogenous with voids (V), and microstructured with voids (M + V). A microstructured sample and the corresponding void distribution are shown in Fig. 1. The homogeneous (H) and microstructured (M) samples are fully dense (100% TMD). The voids in the V and M + V samples are spheres and have diameters of 50 μm. This void size is chosen to allow explicit resolution of each void in the $3 \times 3 \times 15$ mm^3 samples without making the computational time prohibitively expensive. Further discussions on mesh size and computational cost are in Sec. II C. A void volume fraction of 10% is chosen to explicitly capture the effects of porosity on SDT sensitivity. This value is well within the range of 6%–25% pores in the pressed Class III HMX used by Molek et al.[51] Pressed HMX samples often have smaller void diameters and may have a wide range of porosities. Stoltz et al. used ultrasmall angle neutron scattering (USANS) to characterize the internal void structure in RDX (hexahydro-1,3,5-trinitro-1,3,5-triazine) and found void sizes ranging from 1 nm to 20 μm.[52] Mang and Hjelm observed average void sizes of 210–330 nm in pressed TATB (hexahydro-1,3,5-trinitro-1,3,5-triazine) using similar small angle scattering techniques.[53] Skidmore et al. have generated pressed PBX 9501 microstructures with porosities ranging from 0.3% to 21% by volume.[54] Since the reactive burn model parameters described in Sec. II B are calibrated to fully pressed microstructures, the HVRB already accounts for the typical porosity seen in fully dense samples.

A set of five random but statistically similar microstructures is generated using Voronoi tessellation (Fig. 2). These samples conform to the statistical grain size distribution in Fig. 3. This monomodal distribution has a mean grain diameter of 164.7 μm.
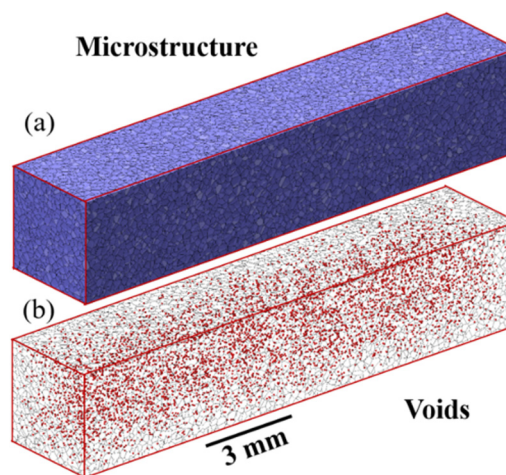
FIG. 1. (a) Three-dimensional microstructure of a sample in the microstructured (M) material case generated by Voronoi tessellation. The sample size is $3 \times 3 \times 15$ mm^3. (b) A random void distribution in the V and V + M cases. The void volume fraction considered is 10% and each void is a sphere with a diameter of 50 μm. The total number of grains is 29 093 in the model shown. The total number of voids is 206 265, giving rise to a void density of 1528 mm^3. Only 5% of the voids are illustrated in (b) for visual clarity.

This grain size distribution approximately corresponds to the Class III pressed HMX used by Molek et al.[51] and Welle et al.,[55] who reported average grain diameters of over 100 μm. This method of microstructure generation results in reasonably realistic, randomized SEMSSs. For the homogenous or microstructured samples with voids, the individual voids are inserted randomly until a total void volume fraction of 10% has been reached or an average void density of 1528/mm^3. For the $3 \times 3 \times 15$ mm^3 samples, this porosity level corresponds to 206 265 voids in each sample. No two voids overlap, ensuring a constant void size and random void distribution. For visual clarity, only 5% of all the voids are shown in Fig. 1(b).

Actual samples in experiments have more heterogeneous characteristics than those in the four sets of samples presented here. For example, nano- and micro-scale voids, microcracks, and directionality of the material properties due to the anisotropic nature of the HMX crystal all play roles in the response of the materials to shock loading. These factors are too small, too complicated, or computationally expensive to be explicitly resolved in the current model setting. They are often ignored in many models reported in the literature. To account for the effects of these factors via grain-level heterogeneities, the density of the HMX for each grain is set to one of three possible values: 80% theoretical maximum density (TMD) (1.52 g/cm^3), 100% TMD (1.90 g/cm^3), and 120% TMD (2.28 g/cm^3). These density variations emulate the effects of local variations in the material and represent one source of variations in fields behind the shock front, normally attributed to localized material heterogeneities. It is important to note that even though 120% TMD is a nonphysical description of a material, this variation in density is used as a modeling tool to account for microstructural aspects not explicitly resolved in this study. It also allows the
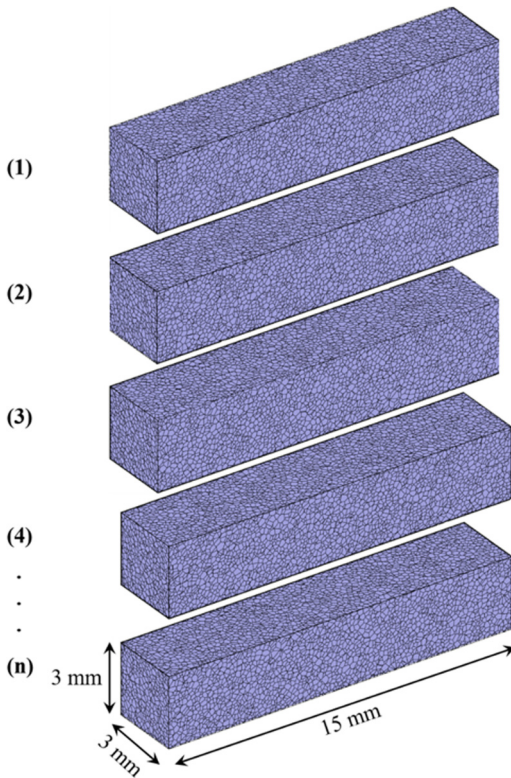
FIG. 2. Statistically equivalent microstructure sample set (SEMSS) for the M and M + V material cases.

average density at the overall sample level and across multiple samples in a SEMSS to conform to the density of the material for samples without voids. Since the HVRB chemistry model used here (further detailed in Sec. II B) is pressure- and density-dependent,
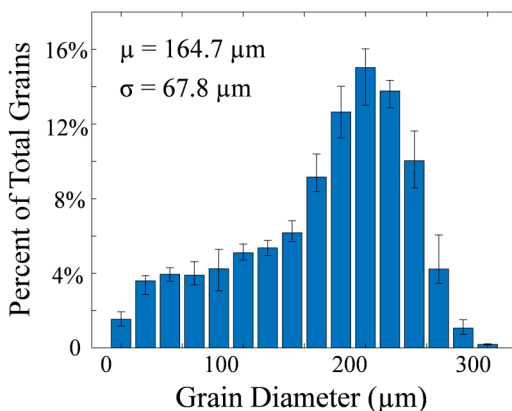

FIG. 3. Monomodal HMX grain size distribution in the statistically equivalent microstructure sample sets of the M and M + V material cases.

the density variations are a source of heterogeneous reaction behavior as well as mechano-thermal behaviors, as seen in experiments. A variation of 20% about the 100% TMD was calibrated based on the work of Hardin et al.,[56] who found the coefficient of variation in the longitudinal stress field in the quasi-steady region behind the stress wave front in polycrystalline HMX (accounting for anisotropy of individual grains) varies from 0.08 to 0.16 at piston velocities around 400 m/s. In this study, the grains are assumed to be perfectly bonded to one another. If two grains with the same density are positioned next to one another, they behave as a single grain of the same density. For the H and V samples, the standard HMX 100% TMD (1.90 g/cm³) is used.

The present framework represents a simplified approach toward explicitly resolving some important features in microstructures of common heterogeneous energetic materials (HEM). While the method of varying the density of the HMX grains may replicate the trends seen in experiments, it is difficult to fully resolve the effect of heterogeneities into a single parameter. Actual experimental samples have more defects not accounted for here, which are known to contribute to hotspot ignition and subsequent detonation.[1,39,57,58] Other HEMs may have a binder and additive components, such as aluminum, which can affect the sensitivity of the material to ignition.[40] It is entirely possible that microstructure heterogeneity plays an even larger role than what is presented in the results of this study. However, as one of the first 3D millimeter macroscale microstructure-explicit and void-explicit modeling approaches, the current framework should be regarded as a step toward fully accounting for the most essential material heterogeneities using mesoscale models.

B. Constitutive relations

The constitutive models used are the same as used by Miller et al.,[50] so only a brief description will be provided here. The specimen is initially stress-free and at rest. A thick aluminum flyer impacts the sample at velocity (U_P) to generate sustained shock loading for the duration of the simulation. The side (lateral) boundaries are constrained in a frictionless manner to maintain the overall conditions of macroscopic uniaxial strain typical of planar impact experiments. The coupled mechanical, thermal, and chemical events in the samples are fully three-dimensional, along with the ME and VE material model.

A simplified Steinberg–Guinan–Lund strain (SGL)-dependent flow stress model is used to account for the viscoplastic constitutive behavior of HMX.[59] This model was previously used by Wood et al. to analyze shock wave localization in porous energetic materials.[16] This strain-rate dependent model is well suited for high strain-rate deformation and accounts for the effects of thermal softening. The material flow stress is calculated via

$$\sigma_Y(\dot{\varepsilon}_P, T) = [\sigma_A + \sigma_T(\dot{\varepsilon}_P, T)], \tag{1}$$

with

$$\dot{\varepsilon}_P = \left\{ \frac{1}{C_1} \exp\left[\frac{2U_K}{T} \left(1 - \frac{\sigma_T}{\sigma_P} \right)^2 \right] + \frac{C_2}{\sigma_T} \right\}^{-1}. \tag{2}$$

TABLE I. HMX material parameters for the SGL flow stress model.

σ_A	C_1	C_2	U_K	σ_P
260 MPa	$3.79 \times 10^{11}\ \text{s}^{-1}$	1.45 Pa s	3000 K	650 MPa

In the above relations, σ_A is the athermal component of the flow stress, σ_T is the thermally activated component of the flow stress, and C_1, C_2, U_K, and σ_P are material parameters. The model has been calibrated by Miller et al.[50] to match the elasto-viscoplastic model used for HMX by Kim et al.[36] which in turn was based on available experimental data. The values of the material parameters in the model are listed in Table I. For further information on this flow stress model or the flow rule, please refer to Sec. II A of Ref. 16.

The bulk response to hydrostatic pressure is modeled using the first order Mie–Grüneisen equation of state (EOS)[60]

$$p = \frac{\rho_0 C_0^2 \left(1 - \frac{\rho_0}{\rho}\right)\left[1 - \frac{\Gamma_0}{2}\left(1 - \frac{\rho_0}{\rho}\right)\right]}{\left[1 - s\left(1 - \frac{\rho_0}{\rho}\right)\right]^2} + \Gamma_0 E, \qquad (3)$$

where p is the pressure, ρ_0 is the initial density of HMX, ρ is the current density of HMX, Γ_0 is the Grüneisen parameter, C_0 is the bulk sound speed, and s is the slope of the Hugoniot. E is the internal energy per unit volume which is found by integrating the specific heat with respect to temperature at constant volume, i.e.,

$$E = \frac{1}{V_0}\int_0^T c_v dT. \qquad (4)$$

The Grüneisen material parameters are listed in Table II and are taken from the CTH material properties library.[61]

The effects of chemical reaction ignition and progression are described using the history variable reactive burn (HVRB)[61] model in the form of

$$\lambda = 1 - \left(1 - \frac{\phi^M}{X}\right)^X, \qquad (5)$$

where

$$\phi = \tau_0^{-1}\int_0^t \left[\frac{(p - p_i)}{p_R}\right]^Z dt. \qquad (6)$$

In the above relations, λ is the extent of reaction, τ_0 is a scaling constant, p is the current pressure, p_i is the threshold pressure for reaction, and p_R, X, M, and Z are reaction rate parameters. Reactive burn models have been widely used to simulate the

TABLE II. HMX material parameters for the Mie–Grüneisen EOS.

ρ_0	C_0	s	Γ_0
1.52 g/cm^3 or 1.90 g/cm^3 or 2.28 g/cm^3	2900 m/s	2.0	1.0

TABLE III. HMX material parameters for the HVRB chemistry model.

τ_0	p_i	p_R	X	M	Z
$1 \times 10^{-6}\ \text{s}$	500 MPa	6 GPa	1	1.5	2.36

ignition and detonation of HEMs.[4,18,19] These empirical models are often calibrated to Pop plot data. As a result, the localized extent of the reaction behind the shock front may not be perfectly resolved (which is a known limitation for the HVRB model). However, with available data and models, this is a reasonable trade-off in order to reach the macroscale from the mesoscale, since the focus here is on analyzing macroscale material behavior, rather than fine details of local fields. The calibration parameters shown in Table III have been fitted to the average state data of HMX and are found in the CTH material properties library.[61]

C. Mesh convergence study

To ensure accurate results for the analysis of the RDD (quantity of interest or QoI), a mesh convergence study is carried out to determine the proper mesh size necessary to explicitly resolve both the grains and voids and to ensure convergence of the QoI. To this end, shock pressure and RDD are calculated for samples including both microstructure and voids (M + V) at mesh sizes ranging from $30\,\mu$m to $5\,\mu$m. The M + V sample set was chosen for this purpose, as it accounts for both types of heterogeneities and, therefore, poses the most stringent requirement for resolution. As shown in Fig. 4, a mesh resolution of $15\,\mu$m is
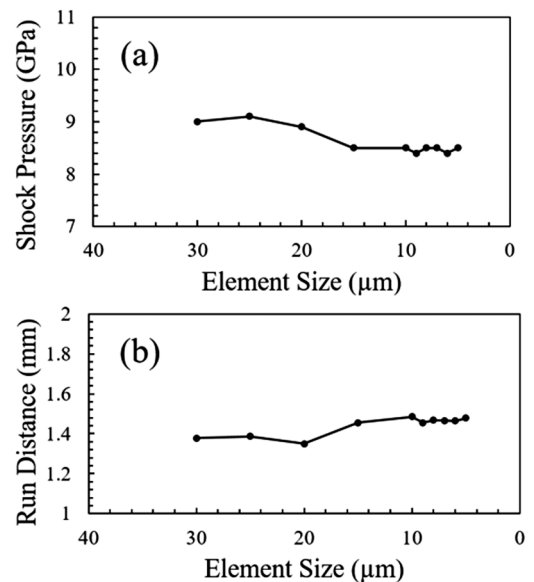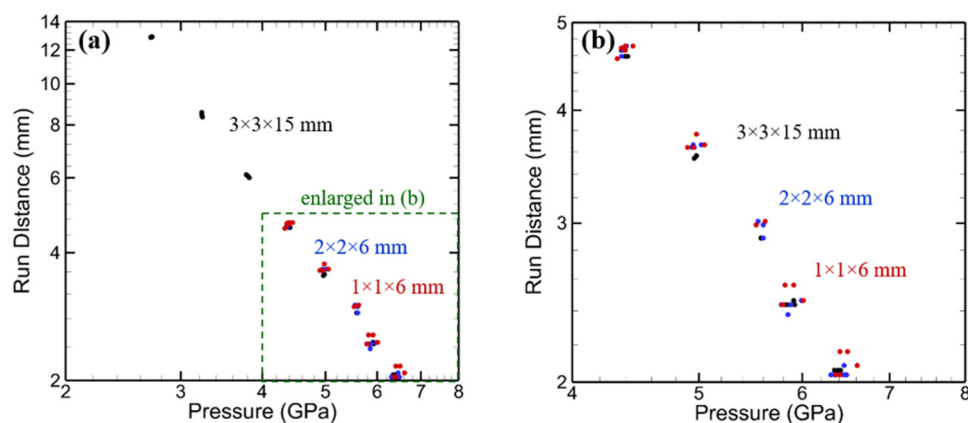

FIG. 4. (a) Shock pressure and (b) run distance to detonation (RDD) for a sample with microstructure and voids (M + V) at mesh resolutions ranging from $30\,\mu$m to $5\,\mu$m.

FIG. 5. (a) Run distance to detonation (RDD) as a function of shock pressure (Pop plot) for the microstructured material case (M) for three different sample sizes: $3 \times 3 \times 15 \text{ mm}^3$, $2 \times 2 \times 6 \text{ mm}^3$, and $1 \times 1 \times 6 \text{ mm}^3$. (b) An enlarged portion of Fig. 5(a).

sufficient to reach convergence for the shock pressure, with further mesh refinement down to $5 \, \mu\text{m}$ resulting in relative fluctuations of ~1.2%. For the RDD, convergence is observed for mesh sizes finer than $10 \, \mu\text{m}$, with further refinement down to $5 \, \mu\text{m}$ resulting in relative fluctuations of ~1.5%. For both the pressure and RDD, the further refinement does not lead to a specific trend (increase or decrease). For this reason, a mesh size of $10 \, \mu\text{m}$ is chosen for all subsequent production calculations. At the resolution of $10 \, \mu\text{m}$, a $3 \times 3 \times 15 \text{ mm}^3$ sample has 1.35×10^8 volumetric elements; at a resolution of $5 \, \mu\text{m}$, the same sample has 1.08×10^9 elements. The computational savings are significant. It is important to note that this study is focused on the macroscale detonation behaviors of the materials, not on details of local fields, as is the case in many other studies. A finer mesh resolution would likely be required to accurately resolve local temperatures. Such local analyses may also appropriately call for the use of an Arrhenius-type chemical reaction rate model, as is commonly the case for small-scale simulations.[3,5,11,62] The HVRB model used here (as outlined in Sec. II B) is a simplified, pressure-dependent chemistry model that does not require direct use of local temperature nor does it account for specific chemical species. It solely tracks the overall extent of reaction.

In addition to the mesh resolution study, an analysis is also carried out on the sample size effects in order to ensure a sufficiently large representative volume element (RVE) for the material while potentially minimizing computational cost. Here, while the smallest microstructure features (voids) dictate the necessary mesh resolution, the largest microstructure features (grains) and the length scale of the SDT process (the run distance to detonation) dictate the necessary RVE size of the sample. As such, in addition to the $3 \times 3 \times 15 \text{ mm}^3$ sample size, smaller sizes are also considered. Although shock pressures as low as ~2.6 GPa with the corresponding RDD of ~13 mm have been simulated, the primary pressure range of interest analyzed is 4–8 GPa. Over this range, the RDD is within 6 mm. Therefore, three smaller sample sizes, $3 \times 3 \times 6 \text{ mm}^3$, $2 \times 2 \times 6 \text{ mm}^3$, and $1 \times 1 \times 6 \text{ mm}^3$, are also used. The run distance to detonation is calculated for four separate shock intensities, the results show strong agreement among the three sizes, indicating that the smaller sample sizes are acceptable. To minimize computational cost without significant loss of accuracy, the remaining calculations are carried out using a sample size of $1 \times 1 \times 6 \text{ mm}^3$ (Fig. 5).

III. RESULTS

A systematic quantification of the effect of the microstructure and voids on the SDT behavior and Pop plot of the pressed HMX is carried out. Section III A discusses how the shock pressure and run distance are determined for each sample. Section III B discusses the effects of microstructure and voids on the Pop plot for 3D samples and compares the results between 3D and similarly generated 2D samples. Finally, Sec. III C presents a thorough statistical framework, which may be used to characterize the detonation behavior over the entire range of shock pressure.

A. Determination of the shock pressure and run distance

The RDD is the longitudinal distance the shock wave travels in the sample before the detonation is fully formed at the shock front. When the material is homogeneous without defects, the detonation begins at the impact face, as this area is subject to the highest loading intensities for the longest period of time. This super-detonation wave propagates through the compressed material faster than the shock wave propagating into the undisturbed material until it reaches the shock front. This is a characteristic of what is commonly referred to as a homogeneous detonation.[63] This type of detonation is often associated with liquid explosives rather than solid explosives.[64,65] In contrast, the detonation wave in materials with microstructure heterogeneity often forms at or close behind the shock front. As the shock wave travels through the material, pore collapse and crack sliding near the shock front may result in subsequent localized shock waves, which strengthen the macroscale shock wave. This behavior is commonly observed for HEM samples containing voids as well as other heterogeneities and is referred to as a heterogeneous detonation.[66,67] For both homogeneous and heterogeneous detonation, the RDD is measured at the distance where the detonation wave begins propagating into the uncompressed material at the shock front.

The relationship between the RDD and the pressure of the imposed shock loading (shock pressure), or the Pop plot, is both material-dependent and microstructure-dependent. This relation can be used to compare the relative SDT sensitivities of different materials and identify microstructure-dependent trends. In the

analysis here, the relations are used to quantify the effects of microstructure and voids of the four HMX cases described earlier. To determine the shock pressure in each simulation, the pressure profile along the entire length of the sample is calculated by averaging the pressures on cross sections perpendicular to the loading direction. The plateau of this profile starting from the impact face is measured and is used to obtain a shock pressure averaged over both sample distance and time. This allows the most accurate assessment of the effective pressure applied as a result of the flyer impact. To calculate the run distance, the location of the shock front in the sample is recorded as a function of time. Since the detonation wave propagates faster than the inert shock wave, the run distance is easily measured by examining the sharp change in the propagation velocity of the shock front. The pressure fields showing shock front locations at four different times in one sample with microstructure and voids (M + V) at an impact of $U_P = 1000$ m/s are shown in Fig. 6. While the detonation front is in the deformed (shocked) material in the first three frames, the detonation front has reached the undeformed material in the fourth frame. The time histories of pressure at nine spatial locations for this sample are shown in Fig. 7. These profiles are useful for comparison with experimental measurements.

It is important to note that the M, V, and M + V simulations carried out here display features of both homogeneous and heterogeneous detonation. The initiation of the detonation begins at void locations and granular interfaces as is expected in a heterogeneous detonation. However, the chemical reaction begins behind the shock front, resulting in a super-detonation wave, which eventually overtakes the shock front. This is a characteristic of homogeneous detonation. There are several possible explanations for this. First, the chemistry model implemented here is pressure-dependent and calibrated to the macroscopic detonation behavior of the bulk material. This simplified model allows us to predict the Pop plot behavior of the material on length scales up to $3 \times 3 \times 15$ mm^3 without making the calculations even more computationally intensive. A more physically accurate chemistry model, such as an Arrhenius-based chemical kinetics model, would likely result in a
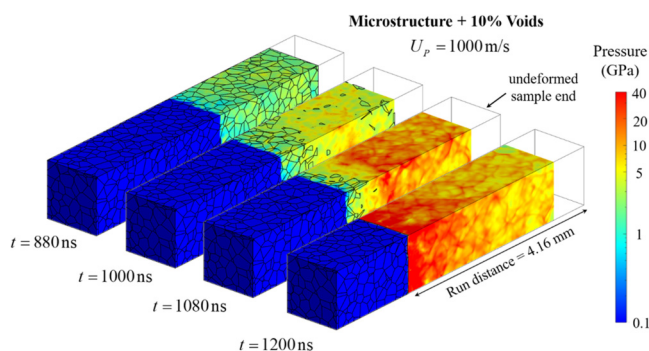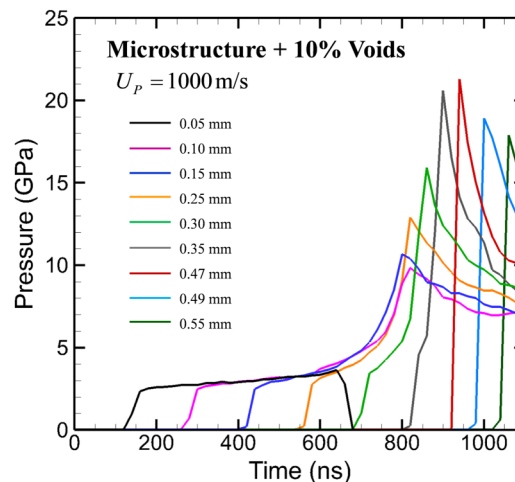
FIG. 7. Time history of pressure at nine locations during the SDT process shown in Fig. 6. Each line represents the average pressure on the cross section perpendicular to the impact direction at a given distance from the impact face.
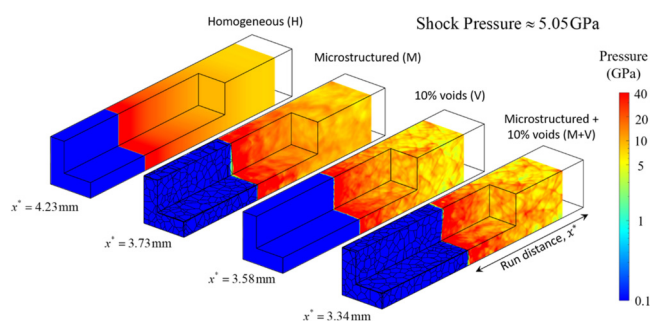
fully heterogeneous detonation behavior. However, the model used here is sufficient to predict the Pop plot behavior, as was demonstrated for 2D samples.[50] Additionally, the void size and distribution used here represent a simplified microstructure setting. Real experimental samples have sub-micrometer voids and their distribution through the sample is far more complicated. The voids considered here indeed contribute to the detonation wave, but the simplified microstructure setting may not embody sufficient heterogeneity to lead to fully heterogeneous detonation. The relatively large void size (a necessary first step to bridge the gap between mesoscale and macroscale simulations) is a possible factor. Further refinement of the microstructure heterogeneity representation, void size, and different reaction models should be considered in the future.

B. Effects of microstructure and voids

In this section, the effects of microstructure heterogeneities are quantified and rank-ordered. The four types of samples described earlier, homogeneous (H), homogeneous with only voids (V), microstructured (M), and microstructured with voids (M + V), are analyzed. A SEMSS with five samples for each of the heterogeneous cases (V, M, and M + V) are used in the analyses. The primary focus is on the effects of the heterogeneities on the Pop plot for 3D samples. For comparison, companion 2D cases for each material case are also analyzed with a corresponding SEMSS. The 2D and 3D SEMSSs have generally matching attributes in terms of grain size, grain size distribution, void size, and void volume fraction (see Figs. 3 and 10). The 2D and 3D results are compared at the end of this section.

The pressure fields in the four material cases at a shock pressure of ~5.05 GPa are shown in Fig. 8. The pressure fields become less uniform as microstructure and voids are introduced, with the M + V case having the most spatial variations. Additionally, the RDD

FIG. 6. The shock-to-detonation transition process in an HMX sample containing both microstructure and voids (10% by volume). The pressure fields are shown on the current (deformed) configurations. Shock loading is due to impact by a thick aluminum flyer at 1000 m/s. The resulting run distance to detonation is 4.16 mm.

FIG. 8. Run-to-detonation distance (RDD) comparison for a sample of each material case under similar pressures. For visual clarity, a cutout of each sample has been removed to show the detonation process in the interior.

decreases as more heterogeneities are introduced, with the M + V case having the shortest RDD.

The Pop plot (relation between the RDD and the shock pressure) for these cases is shown in Fig. 9. Shorter run distances under a given shock pressure suggest higher impact sensitivity and more rapid SDT. It is desirable to not only rank order the Pop plot lines for different material cases but also to quantify the effects of the underlying material mesoscopic factors—microstructure and voids. Also, because of uncertainties or statistical variations resulting from mesoscopic material heterogeneities, the quantification should account for the probabilistic nature of the results. The plot shows both the RDD datasets for the four SEMSSs and the Pop plot lines
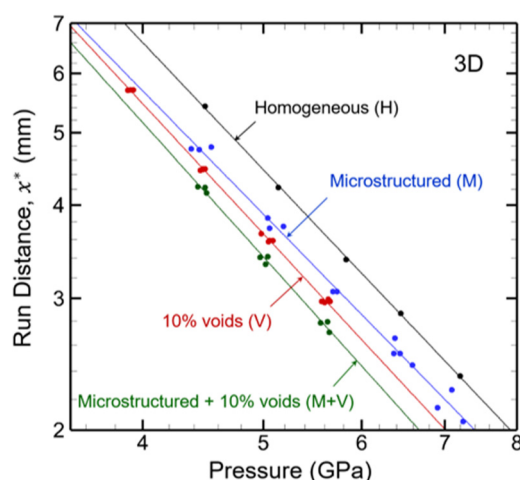
FIG. 9. Run distance to detonation (RDD) as a function of shock pressure (Pop plot) for the four material cases analyzed using 3D simulations. The datasets are: homogeneous (H, black), microstructured (M, blue), homogeneous with 10% voids by volume (V, red), and microstructured with 10% voids (M + V, green). The line for each material case represents the average trend or the conditions for a 50% probability of SDT being observed at that particular pressure and RDD combination. The probability of SDT is higher than 50% above the line and lower than 50% below the line.

that represent the "average" RDD-shock pressure relation for each material case. More specifically, these "average" lines represent the RDD-shock pressure conditions corresponding to a 50% probability of observing SDT. The SDT probability is greater than 50% above the "average" line for a material and less than 50% below the line. For the cases considered, the rank order of the four "average" or 50% lines from the lowest to the highest SDT sensitivity (longest to shortest RDD at the same shock pressure) is: homogeneous (H), microstructured (M), homogenous with voids (V), and microstructured with voids (M + V). To quantify the differences, the average percentage vertical distance between the 50% line for the homogenous (H) case and that for each of the other three cases is calculated and listed in Table IV.

Clearly, the introduction of heterogeneities (microstructure and voids) increases the SDT sensitivity (shifting the Pop plot datasets and Pop plot lines to the lower left in the RDD-pressure space) of the material over the shock pressure regime analyzed. Relative to the homogeneous case, the introduction of 10% voids decreases the average run distance by 18.2%, while the microstructured case on average has a RDD, that is, 12.2% lower than that of the homogeneous case. The material with both microstructure and voids is the most sensitive, with RDDs that are on average 24.3% lower than those of the homogeneous case. Several processes are at play here. The microstructure heterogeneities cause highly inhomogeneous stress and strain fields, thereby giving rise to inhomogeneous and localized temperature rises. Voids lead to sharp spikes in stresses, strains, and temperatures via severe distortion and collapse. The result is the development of hot spots. Note that the levels of these effects are only reflective of the level of material heterogeneities and size scale of the voids considered here. As mentioned in Secs. II C and III A, the HVRB model implemented here is a pressure-dependent model calibrated to experimental run distance data. The effect of heterogeneities on the RDD presented here is likely a conservative estimate of the actual effect of microstructure and voids.

Since most simulations hitherto are carried out in 2D, there is naturally an interest in understanding the potential differences between the two types of models. Three-dimensional models not only can resolve the full 3D nature of the material microstructure and void distributions but also can resolve an additional dimension and level of complexity in the evolution of the thermal, mechanical, and chemical fields. In contrast, 2D models involve more simplifications. Full understanding and quantification of the relations between the two require a much more detailed study than what is possible in the setting of this paper. Nevertheless, we conduct a preliminary analysis here to gain a look at the issue and to illustrate

TABLE IV. Effect of material heterogeneities on the normalized run distance for 3D samples.

SEMSS	Average decrease in RDD relative to H (%)
Homogenous (H)	0
Microstructured (M)	12.2
Homogeneous with 10% voids (V)	18.2
Microstructured with 10% voids (M + V)	24.3

the need for more such analyses. While many factors are at play, our approach involves generating 2D microstructure sample sets (SEMSSs) with statistical attributes that are similar to those of the 3D SEMSSs already analyzed. The "matching" 2D samples are 1×6 mm^2 in size and have an average grain size distribution as shown in Fig. 10 and the same void diameter (50 μm) and void volume fraction (10%). By using similar statistical attributes, we hope to focus on the effects of the additional dimensionality on the material behavior. However, this effort is imperfect, as we can see from Fig. 3 that, owing to the separate SEMSS generation processes in 2D and 3D, there are differences in both the average grain size distribution and the amount of variations among samples in the sets (the error bar). More consistent SEMSS generation, including obtaining 2D samples that are cross sections of the 3D samples, should be considered in the future. Although the specific 2D SEMSSs are different from those in Ref. 50, more details of such 2D simulations are in that paper. The same four material cases as in 3D are considered: homogeneous (H), microstructured without voids (M), homogeneous with voids (V), and microstructured with voids (M + V). The resulting Pop plot from the 2D simulations is shown in Fig. 11, and the average decrease in the normalized run distance relative to the homogenous case is listed in Table V.

There are noticeable differences between the 3D and 2D results (Figs. 9 and 11, respectively) in the heterogeneous (V, M, and M + V) cases, as seen in Fig. 12, while the homogenous (H) case results are essentially the same in 3D and 2D as expected. For the M case, the 3D RDDs that are shorter than the corresponding 2D RDDs. For the V and the M + V cases, the trend is the opposite overall, with significant overlap in the datasets. In all three inhomogeneous material cases, the 2D datasets appear to have wider scatter of the data points than the corresponding 3D datasets. The differences here partially highlight the complexities in comparing 2D and 3D models. One important issue is that representing three-dimensional material microstructures using 2D models invariably leaves out factors that cannot be captured, as 3D is more complex than 2D. As one example, uniformly sized spherical voids (or solid spheres for that matter) appear as circles of various diameters on
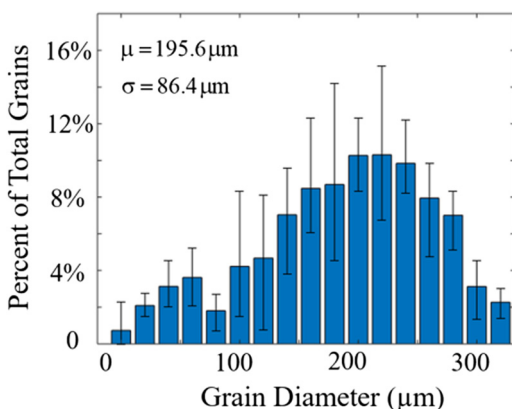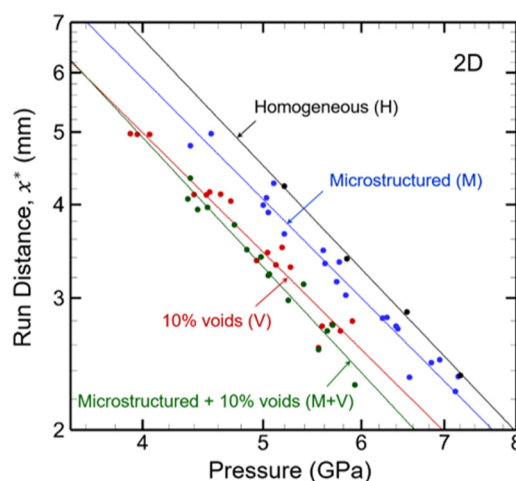

FIG. 11. Run distance to detonation (RDD) as a function of shock pressure (Pop plot) for the four material cases analyzed using 2D simulations. The data sets are: homogeneous (H, black), microstructured (M, blue), homogeneous with 10% voids by volume (V, red), and microstructure with 10% voids (M + V, green). The line for each data set (or material case) represents the average trend or the conditions for a 50% probability of SDT being observed at that particular pressure and RDD combination. The probability of SDT is higher than 50% above the line and lower than 50% below the line.

2D cross sections through the material, as the voids are intercepted by the cross section at different off-center locations, resulting in an extra degree of variation. The same is true for grains or particles. How 2D representations should be developed is a question that needs to be carefully addressed. One potential answer is to use direct cross sections of the 3D samples. However, the size distributions of grains and voids would not be the same as those in the original material. The objective of this discussion here is not to provide answers for the questions, but rather to illustrate the challenges in comparing 2D and 3D models and bring attention to the need for further analyses.

C. Quantification of stochasticity in material response

To quantify the statistical variations in the Pop plot results, a probabilistic formulation is required. To this end, we introduce a

FIG. 10. Monomodal HMX grain size distribution in the statistically equivalent microstructure sample sets of the 2D M and M + V material cases.

TABLE V. Effect of material heterogeneities on the normalized run distance for 2D samples.

SEMSS	Average decrease in RDD relative to H (%)
Homogenous (H)	0
Microstructured (M)	10.1
Homogeneous with 10% voids (V)	22.9
Microstructured with 10% voids (M + V)	27.2
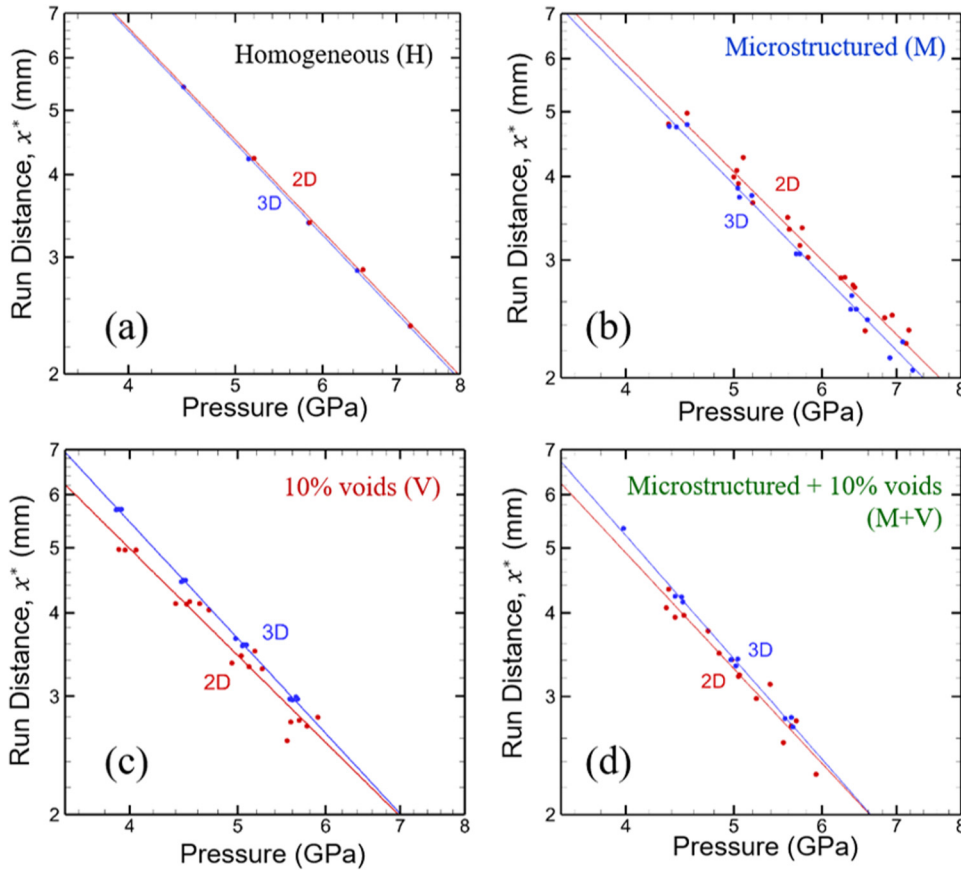
FIG. 12. Comparison of the Pop plots obtained from 2D and 3D simulations. (a) Homogenous (H), (b) microstructured (M), (c) homogenous with 10% voids (V), and (d) microstructured with 10% voids (M + V).

non-dimensional measure in the form of

$$D = \frac{(P_s - P_0)^m (x^* - x_0^*)}{H}, \qquad (7)$$

where H is a material-dependent scaling parameter, m is a dimensionless material-dependent exponent, x^* is the run distance to detonation or RDD in millimeters, and P_s is the shock pressure in GPa. The unit of H takes on the form of GPa^m mm in order to keep D non-dimensional. P_0 is the shock pressure in GPa below which no SDT occurs and x_0^* is the minimum run distance for observing SDT. These quantities should be regarded as material-dependent parameters that constitute bounds for P_s and x^*, respectively. In other words, there is known to be a minimum shock pressure, denoted here as P_0, below which detonation cannot occur, as energy does not localize fast enough to ignite hotspots. Additionally, because chemical ignition cannot occur instantaneously, there must be a minimum time for the shock front to travel before it transforms into a detonation wave. This minimum distance is defined here as x_0^*. This relationship was first proposed by Miller et al.[50] to fully recognize the probabilistic nature of the Pop plot. When $D = 1$, Eq. (7) reduces to a standard power law, which is commonly used to fit data in the pressure-run distance space.[10] This line of best fit corresponds to the

physical space where the SDT is likely to be observed in 50% of samples. Note that SDT has been observed in all recorded samples. The probability here represents the likelihood that SDT has already been observed by the time the shock wave reaches a distance, x^*, from the impact face for a given shock pressure. The non-dimensional D can be considered as the Pop plot number (PPN) which allows the quantification of the probability of observing SDT above or below the "mean" Pop plot line of $D = 1$. Specifically, $D > 1$ and $D < 1$ correspond to conditions for attaining SDT at greater than 50% and less than 50% probabilities, respectively. In order to connect the PPN to a specific probability, a lognormal cumulative distribution function (CDF) is fit to the dataset for each material case (H, V, M, and M + V). Note that the probability here is based on the total number of samples in which SDT was observed in the simulation. A total of 160 simulations were carried out (2D and 3D); however, only the cases where D can be calculated affect the probability distributions shown in Fig. 13. Since the mean value of D is known or set as a unity by definition here, the only remaining parameter in the lognormal distribution to determine via the fit for each material case is the standard deviation σ_d. Since D is non-dimensional, σ_d is also non-dimensional. The results for the 2D and 3D datasets are shown in Fig. 13.
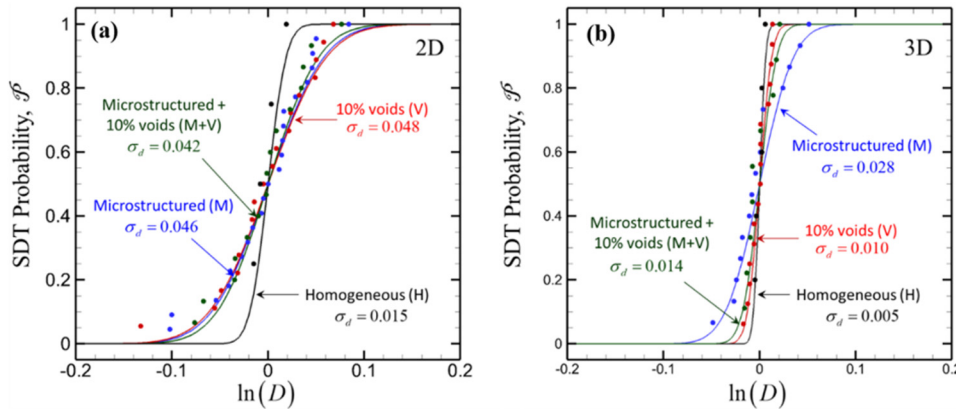
FIG. 13. Cumulative SDT probability obtained from (a) 2D and (b) 3D simulations. The lines are fit to the lognormal cumulative distribution function for the sample sets of the four material cases. The D parameter is computed for each data point using Eq. (7).

Once σ_d has been calculated for each dataset, the corresponding probability map can be generated using

$$\mathscr{P}(P_s, x^\star) = \frac{1}{2} + \frac{1}{2}\text{erf}\left[\frac{1}{\sqrt{2}\sigma_d}(\ln((P_s - P_0)^m) + \ln(x^\star - x_0^\star) - \ln H)\right].$$

(8)

The relation in Eq. (8) is a slightly modified lognormal CDF, where the PPN is treated as the independent variable. A full derivation of this equation can be found in Ref. 50.

The material parameters σ_d, H, and m for the four material cases in both 2D and 3D are shown in Table VI. The conditions for which P_0 and $x_0^\star$ are relevant are outside the pressure regime of 4–8 GPa analyzed here. Accurate determination of values of P_0 and $x_0^\star$ requires separate experimental data or threshold SDT analyses via simulations which are not carried out here. The fitting process shows that their values are low for the datasets here; therefore, for $D = 1$, Eq. (8) essentially approximates the power law for the traditional Pop plot line in Ref. 10. However, the form in Eq. (8) allows datasets to be more accurately determined whenever the relevant threshold data are made available by experiments or separate computations.

TABLE VI. Material parameters for the probabilistic relation in Eq. (8).

Dimensionality	Material case	σ_d	H (GPa^m/mm)	m
3D	Homogeneous (H)	0.005	69.3	1.78
3D	Microstructured (M)	0.028	60.0	1.70
3D	Homogeneous with 10% voids (V)	0.010	66.4	1.85
3D	Microstructured with 10% voids (M + V)	0.014	67.5	1.94
2D	Homogeneous (H)	0.015	77.8	1.82
2D	Microstructured (M)	0.046	56.7	1.64
2D	Homogeneous with 10% voids (V)	0.048	45.5	1.60
2D	Microstructured with 10% voids (M + V)	0.042	54.5	1.74

With Eq. (8), the SDT probability in the entire shock pressure vs RDD space is mapped for each material case. The probability maps for the 2D results are shown in Fig. 14, and the maps for the 3D results are shown in Fig. 15. These figures (and Table VI) show that the microstructure is the primary source of stochasticity in the Pop plot, i.e., the microstructured case (M) has the highest standard deviation. Voids tend to significantly increase the standard deviation in 2D and only slightly increase the standard deviation in 3D. While more systematic analyses are needed to explain why, one conjecture is that 3D samples involve more voids than the 2D samples, thereby "smoothing" out some of the fluctuations in behavior. Another factor may be that the 2D SEMSSs shows more sample-to-sample variations than the 3D SEMSSs, as seen in Figs. 3 and 10.

The probability maps shown here are a useful tool for examining the effects of microstructure heterogeneity on detonation behavior. Equation (8) allows one to calculate the probability for observing SDT at a given run distance under shock loading with a given pressure. Often, it is also desirable to determine the shock pressure required or the minimum run distance necessary to ensure the desired probability of observing SDT. To find the answers to these questions, Eq. (8) can be rearranged to express $\mathscr{P}$ as a function of P_s or $x^\star$, and $x^\star$ as a function of P_s and $\mathscr{P}$, i.e.,

$$P_s(\mathscr{P}, x^\star) = \left\{\frac{H}{(x^\star - x_0^\star)}\exp\left[\sqrt{2}\sigma_d(\text{erf}^{-1}(2\mathscr{P} - 1))\right]\right\}^{1/m} + P_0,$$

(9)

$$x^\star(\mathscr{P}, P_s) = \frac{H}{(P_s - P_0)^m}\exp\left[\sqrt{2}\sigma_d(\text{erf}^{-1}(2\mathscr{P} - 1))\right] + x_0^\star.$$

(10)

These relations are previously derived by Miller et al.[50] and can be used to generate corresponding maps which are not shown here.

D. Probabilistic rank order of Pop plot lines of different material cases

In Figs. 9, 11, and 12, the statistical datasets for different material cases overlap, making the comparison of the run distances of different materials a probabilistic endeavor. More specifically, because the statistical datasets overlap, questions such as "what is the *likelihood* that the run distance of a random 'M + V'
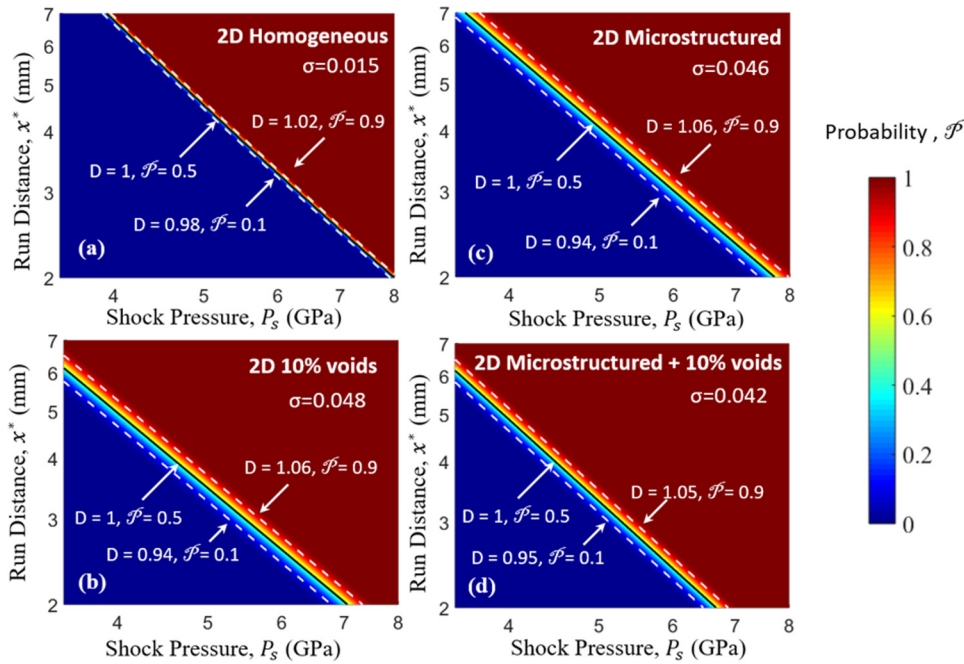
FIG. 14. SDT probability distribution maps for the four material cases obtained using 2D simulations: (a) homogeneous, (b) homogenous with 10% voids, (c) microstructured without voids, and (d) microstructured with 10% voids.

sample is shorter than the run distance of a random 'M' sample?" is of great interest and can only be answered in a probabilistic manner. Graphically, the 50%–50% probability lines for the cases in Figs. 9 and 11 and quantitatively ranked in Tables IV and V only show how the "average" run distances compare "on average" over the entire range of shock pressure of interest. Here, we present a more general approach that allows the run distances of

two random samples of two different materials at any given shock pressure to be compared in a probabilistic manner.

To facilitate the discussion, the probability density function (PDF) distributions of the RDD in the $\mathscr{P} - x^\star$ space for the microstructured (M) and microstructured with voids (M + V) material cases obtained from the 2D simulations are shown in Fig. 16(a). For a given shock pressure P_s, the PDFs are illustrated in Fig. 16(b).
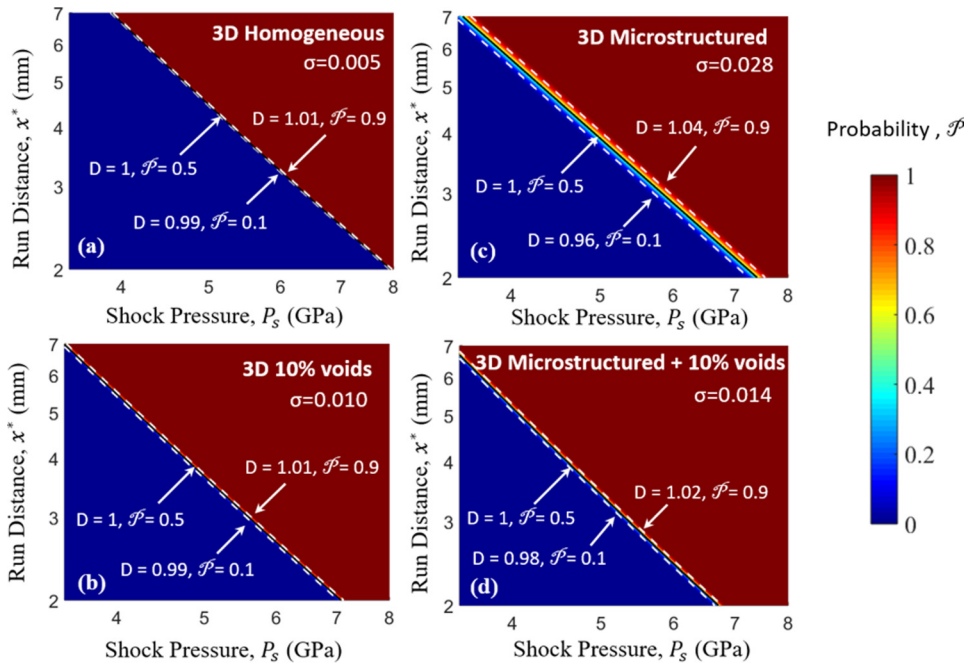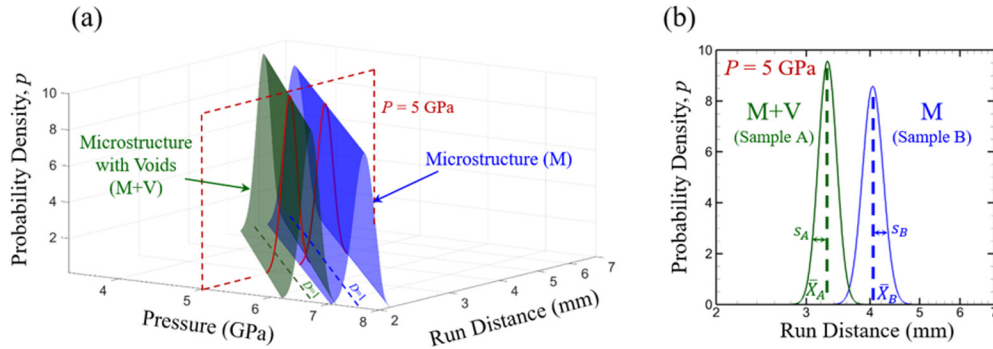

FIG. 15. SDT probability distribution maps for the four material cases obtained using 3D simulations: (a) homogeneous, (b) homogenous with 10% voids, (c) microstructured without voids, and (d) microstructured with 10% voids.

FIG. 16. (a) Distributions of the probability density function (PDF) p of the RDD in the $P - x^*$ space for the microstructured (M) and microstructured with voids (M + V) material cases obtained from the 2D simulations. The function values represent the probability density of observing SDT at different combinations of run distance and shock pressure. (b) A comparison of the PDFs at a shock pressure of 5 GPa for two materials cases. $\bar{X}$ and s represent the sample mean run distance and standard deviation at the given pressure, respectively.

The probabilistic comparison is carried out on such cross sections for different P_s values over the range of interest.

Although the datasets in Fig. 16 are taken from the 2D M + V and M material cases, for the ease of discussion and generality, we will refer to these two cases as "A" and "B," respectively. In the formulas below, the approach described here is applicable to the comparison of any two different materials. At any given shock pressure P_s, the probability density for each material as a function of x^* can be obtained from Eq. (8) as

$$p(x^*; P_s) = \frac{1}{s\sqrt{2\pi}} \exp\left(-\frac{(\ln x^* - \ln X)^2}{2s^2}\right), \tag{11}$$

where

$$X(P_s) = \frac{H}{(P_s - P_0)^m} + x_0^* \tag{12}$$

and

$$s(P_s) = \frac{H\sigma}{(P_s - P_0)^m}. \tag{13}$$

In the above relations, $\bar{X}$ is the mean and s is the standard deviation as illustrated in Fig. 16(b). In this notation, the PDFs for A and B at P_s are denoted as $p_A(x^*; P_s)$ and $p_B(x^*; P_s)$, respectively. The probability of the RDD of A being shorter than the RDD of B for any given shock pressure P_s is

$$\mathscr{P}_{A<B}(P_s) = \int_0^\infty [p_{A<B}(x^*; P_s)]dx^*, \tag{14}$$

where $p_{A<B}(x^*; P_s)$ is the probability density of the RDD of a random sample in distribution A being lower than the RDD of a random sample in distribution B at x^*. This probability density can be evaluated via

$$p_{A<B}(x^*; P_s) = \left[\int_0^{x^*} p_A(x^*; P_s)dx^*\right] \cdot p_B(x^*; P_s), \tag{15}$$

where $\int_0^{x^*} p_A(x^*; P_s)dx^*$ is the probability of observing the RDD of a random sample in A being shorter than or equal to x^*. Since the maximum cumulative probability of any probability density function is unit by definition, $\int_0^{x^*} p_A(x^*; P_s)dx^* \leq 1$ and, therefore,
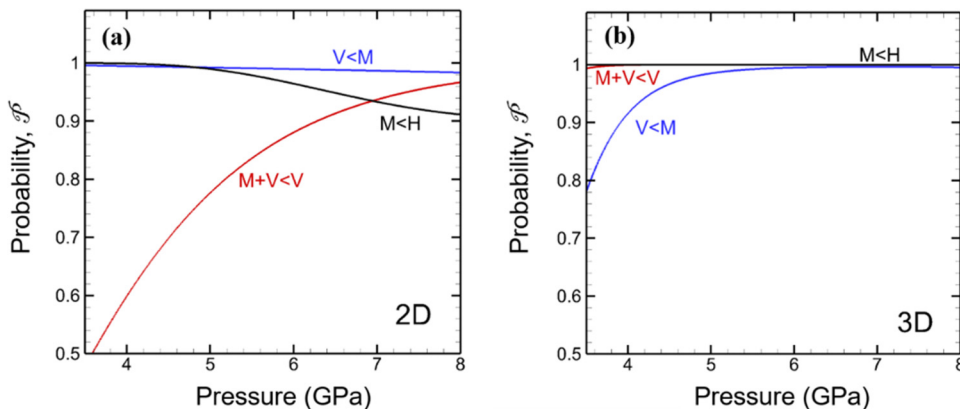
FIG. 17. Probabilities of an M + V sample having a shorter RDD than a V sample (red), a V sample having a shorter RDD than an M sample (blue), and an M sample having a shorter RDD than an H sample (black). Results from (a) 2D simulations and (b) 3D simulations as a function of shock pressure.

$p_{A<B}(x^*; P_s) \leq p_B(x^*; P_s)$. By the same token, $\int_0^\infty p_B(x^*; P_s)dx^* = 1$, which means there exists an upper bound for $\int_0^\infty [p_{A<B}(x^*; P_s)]dx^*$ such that the $\mathscr{P}_{A<B}(P_s)$ evaluated via Eq. (14), satisfies

$$0 \leq \mathscr{P}_{A<B}(P_s) \leq 1. \qquad (16)$$

Equations (14) and (15) are used to compare the RDDs for the four material cases over the entire range of shock pressures studied. The confidence levels for the rank order of $x_{M+V}^* < x_V^* < x_M^* < x_H^*$ are shown in Fig. 17 for both the 2D and the 3D simulations. In the case of the 2D simulations, the confidence level for the M + V samples resulting in shorter RDDs than the V samples increases as the shock pressure increases. In contrast, both the likelihoods for the M samples having shorter RDDs as compared to the H samples and the V samples as compared to the M samples decrease as the shock pressure increases. For the 3D simulations, the confidence level increases as the shock pressure increases for all three comparisons: $x_{M+V}^* < x_V^* < x_M^* < x_H^*$. Again, more systematic studies are required to explain why 2D and 3D simulations are different.

IV. CONCLUSION

There is a long-standing interest in three-dimensional (3D) simulations of the behavior of energetic materials and in understanding potential differences between 2D and 3D simulations. While 2D simulations have been extensively carried out at the micrometer to tens-of-micrometers size scales, simulations at the millimeter scale explicitly accounting for microstructure and voids are rare. 3D simulations at the millimeter scale are equally sparse. In this paper, we simulate the shock-to-detonation transition (SDT) process of pressed HMX using three-dimensional, microstructure-explicit, and void-explicit mesoscale models. We find homogeneous HMX samples to be the least sensitive to detonation (having the longest RDD or requiring the highest shock pressure to show SDT under otherwise identical conditions). As material heterogeneities are successively introduced, the RDD decreases for a given shock pressure. While both voids and granular microstructure are found to significantly affect the SDT process, voids are observed to play a more dominate role than granular microstructure in increasing the SDT sensitivity. The material with both microstructure and 10% voids has the lowest average run distance which is 24.3% lower relative to that of the homogeneous material.

For comparison purposes, 2D simulations are also carried out to assess the differences between the 2D and 3D simulations. The 2D and 3D models yielded results that are overall consistent with each other, but with significant differences. In general, the 2D simulations exhibit wider scatter of the RDD in all material cases than the 3D simulations. To expand on this analysis, a new probabilistic formulation is presented to rank order the effects of microstructure and voids in the 2D and 3D results. A pressure dependence is observed where the effects of voids are more pronounced under higher shock pressures. There is a high level of confidence that microstructure plays an important role in all 3D SDT simulations, but that confidence decreases slightly for 2D samples at high shock pressures. This comparison illustrates the complexities of the 2D vs 3D issue and points out the need for more systematic analyses in

the future, including a more consistent generation of the 2D and 3D SEMSSs.

REFERENCES

[1]S. Kim et al., "Prediction of shock initiation thresholds and ignition probability of polymer-bonded explosives using mesoscale simulations," J. Mech. Phys. Solids **114**, 97–116 (2018).

[2]A. Barua, "Mesoscale computational prediction and quantification of thermo-mechanical ignition behavior of polymer-bonded explosives (PBXs)," Ph.D. thesis (Georgia Institute of Technology, 2013).

[3]C. Yarrington, R. R. Wixom, and D. L. Damm, *Mesoscale Simulations Using Realistic Microstructure and First Principles Equation of State* (Sandia National Laboratory, Albuquerque, NM, 2012).

[4]M. R. Baer, "Modeling heterogeneous energetic materials at the mesoscale," Thermochim. Acta **384**(1–2), 351–367 (2002).

[5]R. N. Mulford and D. C. Swift, "Mesoscale modelling of shock initiation in HMX-based explosives," AIP Conf. Proc. **620**, 415–418 (2002).

[6]J. J. Rimoli, E. Gürses, and M. Ortiz, "Shock-induced subgrain microstructures as possible homogenous sources of hot spots and initiation sites in energetic polycrystals," Phys. Rev. B **81**(1), 014112 (2010).

[7]J. G. Bennett et al., "A constitutive model for the non-shock ignition and mechanical response of high explosives," J. Mech. Phys. Solids **46**(12), 2303–2322 (1998).

[8]D. J. Benson and P. Conley, "Eulerian finite-element simulations of experimentally acquired HMX microstructures," Modell. Simul. Mater. Sci. Eng. **7**(3), 333–354 (1999).

[9]P.T. Rao and K. A. Gonthier, "Analysis of dissipation induced by successive planar shock loading of granular explosive," in *51st AIAA/SAE/ASEE Joint Propulsion Conference, Orlando, FL* (AIAA, 2015).

[10]J. Ramsay and A. Popolato, *Analysis of Shock Wave and Initiation Data for Solid Explosives* (Los Alamos Scientific Laboratory, University of California, Albuquerque, NM, 1965).

[11]K. J. Laidler, "The development of the Arrhenius equation," J. Chem. Educ. **61**(6), 494 (1984).

[12]H. K. Springer et al., "Investigating short-pulse shock initiation in HMX-based explosives with reactive meso-scale simulations," J. Phys. Conf. Ser. **500**(5), 052041 (2014).

[13]C. Tarver and C. May, "Short pulse shock initiation experiments and modeling on LX-16, LX-10, and ultrafine TATB," in *Fourteenth International Detonation Symposium* (IDS, 2010).

[14]C.-G. Zhan and D. A. Dixon, "A density functional theory approach to the development of Q− e parameters for the prediction of reactivity in free-radical copolymerizations," J. Phys. Chem. A **106**(43), 10311–10325 (2002).

[15]C. M. Tarver, "Chemical energy release in self-sustaining detonation waves in condensed explosives," Combust. Flame **46**, 157–176 (1982).

[16]M. A. Wood et al., "Multiscale modeling of shock wave localization in porous energetic material," Phys. Rev. B **97**(1), 014109 (2018).

[17]C. L. Mader, *Two Dimensional Homogeneous and Heterogeneous Detonation Wave Propagation* (Los Alamos Scientific Laboratory, Albuquerque, NM, 1976).

[18]E. L. Lee and C. M. Tarver, "Phenomenological model of shock initiation in heterogeneous explosives," Phys. Fluids **23**(12), 2362–2372 (1980).

[19]R. Menikoff and M. S. Shaw, "Reactive burn models and ignition & growth concept," EPJ Web Conf. **10**, 00003 (2010).

[20]C. L. Mader, *Numerical Modeling of Explosives and Propellants*, 2nd ed. (CRC Press, 1998).

[21]R. Menikoff and M. S. Shaw, "Review of the forest fire model for high explosives," Combust. Theory Modell. **12**(3), 569–604 (2008).

[22]J. N. Johnson, P. K. Tang, and C. A. Forest, "Shock-wave initiation of heterogeneous reactive solids," J. Appl. Phys. **57**(9), 4323–4334 (1985).

[23]E. Hertel *et al*, "CTH: A software family for multi-dimensional shock physics analysis," in *Shock Waves@ Marseille I* (Springer, 1995), pp. 377–382.

[24]J. M. McGlaun, S. L. Thompson, and M. G. Elrick, "CTH: A three-dimensional shock wave physics code," Int. J. Impact Eng. **10**(1), 351–360 (1990).

[25]S. K. Chidester, K. S. Vandersall, and C. Tarver, *Shock Initiation of Damaged Explosives* (LLNL, 2009).

[26]C. M. Tarver, "Chemical kinetic modeling of HMX and TATB laser ignition tests," J. Energ. Mater. **22**(2), 93–107 (2004).

[27]A. L. Nichols and C. M. Tarver, "A statistical hot spot reactive flow model for shock initiation and detonation of solid high explosives," in *Twelfth International Symposium on Detonation, San Diego, CA* (Office of Naval Research, 2002).

[28]R. V. Browning and R. J. Scammon, "Microstructural model of ignition for time varying loading conditions," AIP Conf. Proc. **620**, 987–990 (2002).

[29]B. F. Henson *et al.*, "Ignition chemistry in HMX from thermal explosion to detonation," AIP Conf. Proc. **620**, 1069–1072 (2002).

[30]J. Massoni *et al.*, "A mechanistic model for shock initiation of solid explosives," Phys. Fluids **11**(3), 710–736 (1999).

[31]A. K. Kapila *et al.*, "Two-phase modeling of deflagration-to-detonation transition in granular materials: Reduced equations," Phys. Fluids **13**(10), 3002–3024 (2001).

[32]A. Barua and M. Zhou, "A Lagrangian framework for analyzing microstructural level response of polymer-bonded explosives," Modell. Simul. Mater. Sci. Eng. **19**(5), 055001 (2011).

[33]A. Barua *et al.*, "Ignition criterion for heterogeneous energetic materials based on hotspot size-temperature threshold," J. Appl. Phys. **113**(6), 064906 (2013).

[34]A. Kapahi and H. S. Udaykumar, "Three-dimensional simulations of dynamics of void collapse in energetic materials," Shock Waves **25**(2), 177–187 (2015).

[35]N. K. Rai, "Numerical framework for mesoscale simulation of heterogeneous energetic materials," Ph.D. thesis (University of Iowa, 2015).

[36]S. Kim *et al.*, "Computational prediction of probabilistic ignition threshold of pressed granular octahydro-1,3,5,7-tetranitro-1,2,3,5-tetrazocine (HMX) under shock loading," J. Appl. Phys. **120**(11), 115902 (2016).

[37]M. R. Lambrecht *et al.*, "Electromagnetic modeling of hot-wire detonators," IEEE Trans. Microwave Theory Tech. **57**(7), 1707–1713 (2009).

[38]L. E Fried *et al.* "The role of viscosity in TATB hot spot ignition," AIP Conf. Proc. **1426**, 299 (2012).

[39]Y. Wei *et al.*, "Quantification of probabilistic ignition thresholds of polymer-bonded explosives with microstructure defects," J. Appl. Phys. **124**(16), 165110 (2018).

[40]C. Miller *et al.*, "Ignition thresholds of aluminized HMX-based polymer-bonded explosives," AIP Adv. **9**(4), 045103 (2019).

[41]N. K. Rai, M. J. Schmidt, and H. S. Udaykumar, "High-resolution simulations of cylindrical void collapse in energetic materials: Effect of primary and secondary collapse on initiation thresholds," Phys. Rev. Fluids **2**(4), 043202 (2017).

[42]R. A. Austin *et al.*, "Direct numerical simulation of shear localization and decomposition reactions in shock-loaded HMX crystal," J. Appl. Phys. **117**(18), 185902 (2015).

[43]R. A. Austin *et al.*, "Modeling pore collapse and chemical reactions in shock-loaded HMX crystals," J. Phys. Conf. Ser. **500**(5), 052002 (2014).

[44]C. D. Yarrington, R. R. Wixom, and D. L. Damm, "Shock interactions with heterogeneous energetic materials," J. Appl. Phys. **123**(10), 105901 (2018).

[45]M. Baer, M. Kipp, and F. V. Swol, *Micromechanical Modeling of Heterogeneous Energetic Materials* (Sandia National Laboratories, Albuquerque, NM, 1998).

[46]J. Reaugh, "Grain-scale dynamics in explosives," Lawrence Livermore National Laboratory Technical Report No. UCRL-ID-150388-2002, 2002.

[47]N. K. Rai and H. S. Udaykumar, "Three-dimensional simulations of void collapse in energetic materials," Phys. Rev. Fluids **3**(3), 033201 (2018).

[48]T. L. Jackson *et al.*, "Multi-dimensional mesoscale simulations of detonation initiation in energetic materials with density-based kinetics," Combust. Theory Modell. **22**(2), 291–315 (2018).

[49]Y. Wei *et al.*, "Integrated Lagrangian and Eulerian 3D microstructure-explicit simulations for predicting macroscopic probabilistic SDT thresholds of energetic materials," Comput. Mech. **64**, 547 (2019).

[50]C. Miller *et al.*, "Prediction of probabilistic Pop plot via millimeter-scale microstructure-explicit and void-explicit simulations," Prop. Explos. Pyrotech. **45**, 254 (2020).

[51]C. D Molek *et al.*, "Microstructural characterization of pressed HMX material sets at differing densities," in *19th Biennial American-Physical-Society (APS) Conference on Shock Compression of Condensed Matter (SCCM), Tampa, FL* (American Institute of Physics, 2015).

[52]C. A. Stoltz, B. P. Mason, and J. Hooper, "Neutron scattering study of internal void structure in RDX," J. Appl. Phys. **107**(10), 103527 (2010).

[53]J. T. Mang and R. P. Hjelm, "Fractal networks of inter-granular voids in pressed TATB," Prop. Explos. Pyrotech. **38**(6), 831–840 (2013).

[54]C. Skidmore *et al.*, *The Evolution of Microstructural Changes in Pressed HMX Explosives* (Los Alamos National Laboratory, Albuquerque, NM, 1998).

[55]E. J. Welle *et al.*, "Microstructural effects on the ignition behavior of HMX," J. Phys. Conf. Ser. **500**(5), 052049 (2014).

[56]D. B. Hardin, J. J. Rimoli, and M. Zhou, "Analysis of thermomechanical response of polycrystalline HMX under impact loading through mesoscale simulations," AIP Adv. **4**(9), 097136 (2014).

[57]K. Ramos, M. Cawkwell, and D. Hooks, "Defect characterization and the effect of pre-existing and shock-induced defects on the shock response of single crystal explosives," in *17th Biennial International Conference of the APS Topical Group on Shock Compression of Condensed Matter, Chicago, IL* (Bulletin of the American Physical Society, 2011).

[58]C. Hua *et al.*, "Research on the size of defects inside RDX/HMX crystal and shock sensitivity," Prop. Explos. Pyrotech. **38**(6), 775–780 (2013).

[59]D. J. Steinberg and C. M. Lund, "A constitutive model for strain rates from 10^{-4} to 10^6 s^{-1}," J. Appl. Phys. **65**(4), 1528–1533 (1989).

[60]E. Grüneisen, *Handbuch der Physik* (Verlag Julius Springer, Berlin, 1926).

[61]G. I. Kerley, "CTH equation of state package: Porosity and reactive burn models," Sandia National Laboratories Report No. SAND92-0553, 1992.

[62]A. Tokmakoff, M. D. Fayer, and D. D. Dlott, "Chemical-reaction initiation and hot-spot formation in shocked energetic molecular materials," J. Phys. Chem. **97**(9), 1901–1913 (1993).

[63]C. L. Mader, *Numerical Modeling of Detonations*, Los Alamos Series in Basic and Applied Sciences (Berkeley University of California Press, 1979).

[64]C. A. Handley *et al.*, "Understanding the shock and detonation response of high explosives at the continuum and meso scales," Appl. Phys. Rev. **5**(1), 011303 (2018).

[65]A. W. Campbell, W. C. Davis, and J. R. Travis, "Shock initiation of detonation in liquid explosives," Phys. Fluids **4**(4), 498–510 (1961).

[66]H. W. Hubbard and M. H. Johnson, "Initiation of detonations," J. Appl. Phys. **30**(5), 765–769 (1959).

[67]C. L. Mader, "Initiation of detonation by the interaction of shocks with density discontinuities," Phys. Fluids **8**(10), 1811–1816 (1965).